Tropical Cyclone Size Change under Ocean Warming and Associated Responses of Tropical Cyclone Destructiveness: Idealized Experiments

Zanmin XU[1], Yuan SUN[2,1*], Tim LI[1,3], Zhong ZHONG[2], Jia LIU[1], and Chen MA[1]

1 *Key Laboratory of Meteorological Disaster, Ministry of Education (KLME)/Joint International Research Laboratory of Climate and Environmental Change (ILCEC)/Collaborative Innovation Center on Forecast and Evaluation of Meteorological Disasters (CIC-FEMD), Nanjing University of Information Science &Technology, Nanjing* 210044, *China*

2 *College of Meteorology and Oceanography, National University of Defense Technology, Nanjing* 211101, *China*

3 *Department of Atmospheric Sciences, School of Ocean and Earth Science and Technology, University of Hawaii, Honolulu, HI* 96822, *USA*

(Received March 18, 2019; in final form October 16, 2019)

ABSTRACT

The power dissipation index (PDI), which is defined as the sum of the cube of tropical cyclone (TC) maximum wind speed during TC lifetime, is widely used to estimate the TC destructive potential. However, due to the lack of high-resolution observations, little attention has been paid to the contribution of TC size change to TC destructive potential in response to ocean warming. In this study, sensitivity experiments are performed by using the high-resolution Weather Research and Forecasting (WRF) model to investigate the responses of TC size and TC destructive potential to prescribed sea surface temperature (SST) increase under the present climate condition. The results show that TC size increases with the ocean warming. Possible reasons for TC size change are investigated with a focus on the outer air–sea moisture difference (ASMD). As SST increases, ASMD in the outer zone of the TC is larger than that in the inner zone, which increases the surface entropy flux (SEF) of the outer zone. This change in the radial distribution of SEF causes the increase of tangential wind in the outer zone, which further increases SEF, resulting in a positive feedback between outer-zone SEF and outer-zone tangential wind. This feedback leads to the increase of the radius of gale-force wind, leading to the expansion of TC size. Moreover, to estimate the contribution of TC size change to TC destructiveness, we calculate TC size-dependent destructive potential (PDS) as the storm size information is available in the model outputs, as well as PDI that does not consider the effect of TC size change. We find that PDS increases exponentially as SST increases from 1 to 4°C, while PDI increases linearly; hence the former is soon much greater than the latter. This suggests that the growth effect of TC size cannot be ignored in estimating destructiveness under ocean warming.

Key words: tropical cyclone destructive potential, tropical cyclone size, surface entropy flux, air–sea moisture difference, sea surface temperature

Citation: Xu, Z. M., Y. Sun, T. Li, et al., 2020: Tropical cyclone size change under ocean warming and associated responses of tropical cyclone destructiveness: Idealized experiments. *J. Meteor. Res.*, **34**(1), 163–175, doi: 10.1007/s13351-020-8164-4.

1. Introduction

Impact of global warming on tropical cyclone (TC) properties and activities in terms of duration, frequency, intensity, and size remains a hot topic (Chan and Liu, 2004; Li et al., 2010; Walsh et al., 2015). Due to the large natural variability in TC activity over the western North Pacific (WNP) and the difficulty of quantifying the contribution to changes of TC activity by natural variability with relatively short observation records, debates continue regarding whether or not the observed TC activity changes are linked to global warming (Webster et al., 2005; Klotzbach, 2006; Walsh et al., 2015).

It is known that global warming impacts TC activity mainly via the ocean, specifically via sea surface temperature (SST) (Lighthill et al., 1994; Deo et al., 2011;

Supported by the National Key Research and Development Program of China (2018YFC1505803), National Natural Science Foundation of China (41605072), Natural Science Foundation of Jiangsu Province (BK20160768), and Priority Academic Program Development (PAPD) of Jiangsu Higher Education Institutions.

*Corresponding author: sunyuan1214@126.com.

Bacmeister et al., 2018; Li and Sriver, 2018) and upper-ocean heat content (Lin et al., 2013; Trenberth et al., 2018). The US Climate Change Science Program 3.3 report noted that "human-induced greenhouse gas increases have very likely contributed to the increase in SSTs in hurricane formation regions" (Knutson et al., 2010). Due to limited observation data length on TCs, many studies on the impact of global warming on TC activity were carried out using global or regional models, including using the model outputs of the Coupled Model Intercomparison Project phase 5 (CMIP5). For future projections of TC activity, we only have model outputs. CMIP5 archives the outputs of about 30 coupled general circulation models (GCMs); in most cases, each model provides outputs from a historical run and two future warming scenarios (representative concentration pathways 4.5 and 8.5, namely, RCP4.5 and RCP8.5) (Taylor et al., 2012). Zhang and Wang (2017) used a pseudo global warming method to investigate future projections under RCP4.5 and RCP8.5. Their results indicated that in a warmer climate, the number of strong TCs in the Pacific Ocean would increase. However, the low resolution of climate models cannot resolve the structure of TC inner core. Therefore, studies on how ocean warming will affect TC size are limited.

Some recent studies indicated that the change of TC size due to ocean warming is not negligible. Radu et al. (2014) pointed out that TC size increases proportionally to the surface latent heat flux as air temperature and SST increase, which was based on a high-resolution model simulation of one TC case. Wang et al. (2015) presented a physically based analytic model to characterize the wind profile of TC. In their simulations, TC size was sensitive to SST increase and to the initial vortex structure. Chavas et al. (2016) indicated that the mean TC size increases systematically with relative SST (defined as the difference between local SST and tropical mean SST). Sun et al. (2013, 2014) noted that TC size increases obviously as SST increases, based on case studies. However, due to the relatively coarse resolution (20 km) in their regional climate model, the storm structure was not well resolved; thus, it was impossible to explain the change of TC size using the dynamic and thermodynamic processes of the storm structure, which are vital to the change of TC activities. Sun et al. (2017a) suggested that the increase of TC size due to SST increase may play a critical role in the estimated change of size-dependent destructive potential; however, the influence of TC track on TC size could not be excluded in their experiments as the simulated TC turned northward earlier as SST increased.

Besides, studies have illustrated that the effects of inner and outer regions on TC intensity and size are different. Chan and Chan (2015) examined that inner-core-induced intensification mainly results from the inner-core dynamics. Xu and Wang (2010a) showed that surface entropy flux (SEF) further outward contributes little to TC intensity. Sun et al. (2014) illustrated that the increase of outer SST reinforces the activity of outer spiral rainbands, which makes the outer SST responsible for smaller change in TC intensity. Hill and Lackmann (2009) reported that latent heat release in outer rainbands can result in the expansion of outer wind field. Thereby, large-scale ocean warming is likely to affect the convection in the outer region (e.g., outer spiral rainbands) and thus may eventually lead to the increase of TC size. However, this needs to be further scrutinized by using high-resolution data before we can have high confidence on such a conclusion. In this study, we design a set of high-resolution (3 km) sensitivity experiments using an atmosphere model and present-day climatological state, to study the impact of ocean warming on TC destructive potential considering TC size change, and to reveal related mechanisms behind the TC size change during the dynamic and thermodynamic processes of storm structure development.

The paper is organized as follows. Data, model, and experimental design are briefly introduced in Section 2. The results of our model simulations and analyses are presented in Section 3. Finally, a short summary and discussion are given in Section 4.

2. Data, methods, and model configuration

The Weather Research and Forecasting (WRF-ARW) model (version 3.8.1) is used to examine the sensitivity of TC size and destructive potential to SST increase in the WNP. The model is configured with three domains of horizontal resolutions of 27, 9, and 3 km, respectively, with the same 41 levels in the vertical. The first domain (d01) is centered at (30°N, 140°E) with 299 × 249 grids, which covers nearly the entire WNP; the second domain (d02) has 211 × 211 grids, and the third domain (d03) has 300 × 300 grids covering majority of the TC region. Note that the second and third domains automatically follow the movement of the model storm center via an automatic vortex-following algorithm. The model domains are shown in Fig. 1a.

The control experiment (CTRL) is initialized with a 10-yr (2001–2010) seasonal (July–November) mean climatology. The 1° × 1° NCEP Final Analysis (FNL) data are used to calculate the climatology. The SST in the sensitivity experiments is spatially uniformly increased by 1, 2, 3, and 4°C in all three domains with respect to

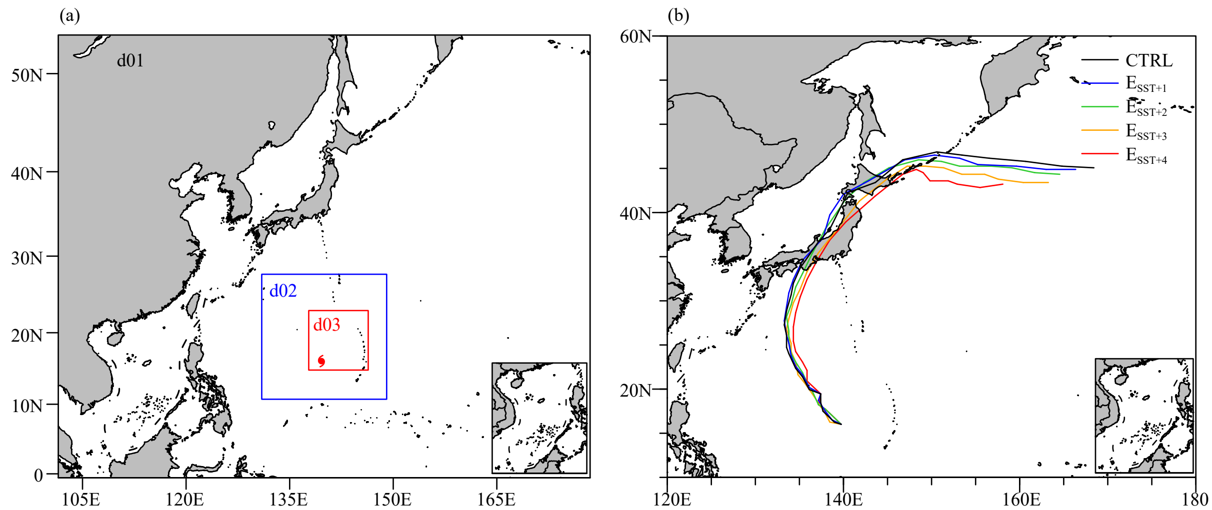

Fig. 1. (a) WRF nested domain configuration for idealized simulations and (b) storm tracks of all experiments. Note that the red storm symbol in (a) represents the initial tropical storm location.

CTRL, which are referred to as Exps E_{SST+1}, E_{SST+2}, E_{SST+3}, and E_{SST+4}, respectively. Then, using the Bogus scheme that comes with the WRF model, we add a Rankine vortex as the tropical storm centered at (16.1°N, 139.6°E), which has a radius of 90 km and a maximum sustained wind speed of 12 m s^{-1}. This location is chosen because it is the 10-yr mean site for TC genesis in the WNP during the TC season of July–November. The first and second domains of the model include a WRF single-moment 6-class (WSM6) microphysics scheme (Hong et al., 2004), the Kain–Fritch convective scheme (Kain, 2004), the Goddard scheme for shortwave radiation processes (Chou and Suarez, 1994), and the Rapid Radiative Transfer Model (RRTM) for longwave radiation processes (Mlawer et al., 1997). The third domain uses the same settings except for the cumulus parameterization scheme. Note that the design of this study is different from that of Sun et al. (2017a). In this study, we use idealized cases based on the present-day climatology, which is expected to draw more universal conclusions about the impact of ocean warming on TC size change and destructiveness; whereas simulations of real cases are carried out in Sun et al. (2017a).

The TC destructive potential is a better parameter to represent the potential of TC destruction than TC intensity or TC frequency when used alone. In previous studies (Emanuel, 2005; Sun et al., 2017a), both power dissipation index (PDI) and TC size-dependent destructive potential (PDS) were used to estimate TC destructive potential. Note that PDS is a TC destructive potential index that considers TC size. The PDI is defined as the sum of the cube of maximum wind speed during the lifetime of the TC [Eq. (1)]. The PDS is calculated by using gale-force (> 17 m s^{-1}) wind near the TC core and over the TC lifetime [Eq. (2)]. The advantage of using the PDS is that it takes into account the impact of TC size on the basis of the PDI. In the past, there were no reliable long-term records on TC size due to the lack of measurement tools. As a result, it was difficult to consider TC size as part of the PDI. Thanks to high-resolution numerical model outputs, we can now see the inner structure of TC and estimate TC size properly. In this study, we use high-resolution model outputs to calculate PDI and PDS as follows:

$$\mathrm{PDI} = \int_0^{\tau} V_{\max}^3 \mathrm{d}t, \tag{1}$$

$$\mathrm{PDS} = \int_0^{\tau}\int_0^{A_0} C_{\mathrm{D}}\rho|\boldsymbol{V}|^3 \mathrm{d}A\mathrm{d}t, \tag{2}$$

where $V_{\max}$ is 10-m maximum sustained wind speed, $|\boldsymbol{V}|$ is the magnitude of 10-m surface wind, ρ is surface air density, C_{D} is surface drag coefficient, A_0 is the area of gale-force wind, and τ is the lifetime of the TC.

Although PDI and PDS can be directly calculated with the high-resolution model outputs, the aim of this study is to not only obtain these values but also further quantify the contributors to the changes of PDI/PDS. Emanuel (2007) inferred that PDI can be deconvolved into two terms, i.e., $\ln(\mathrm{PDI}) = \ln(L) + \ln(I)$, where L is rescaled TC lifetime [defined in Eq. (3) below] and I is rescaled TC intensity [defined in Eq. (4)]. Following this idea, Sun et al. (2017a) added a term to calculate the contribution of TC size to PDS as, $\ln(\mathrm{PDS}) = \ln(L) + \ln(I) + \ln(S)$, where S is rescaled TC size defined in Eq. (5).

$$L = \frac{\int_0^{\tau} V_{\max}\mathrm{d}t}{V_{\mathrm{smax}}}, \tag{3}$$

$$I = \frac{\int_0^{\tau} V_{\max}^3 \mathrm{d}t}{L}, \tag{4}$$

$$S = \frac{\mathrm{PDS}}{I \times L} = \frac{\int_0^{\tau}\int_0^{A_0} C_{\mathrm{D}}\rho|\boldsymbol{V}|^3 \mathrm{d}A\mathrm{d}t}{I \times L}. \tag{5}$$

Here, V_{smax} is lifetime peak intensity of the TC. Through rescaling TC lifetime, intensity, and size using V_{smax}, we have a more unified and standardized way to characterize the TCs of different duration, strength, and size at various moments, though this is not optimal (Emanuel, 2007). Based on Eqs. (1)–(5), we can estimate the relative contributions of L, I, and S to PDS changes.

3. Results

3.1 *Change of TC size under ocean warming*

As the SST increases uniformly by 1 to 4°C, both increased maximum wind speed (MWS) and reduced minimum sea level pressure (MSLP) indicate that the TC turns stronger with increasing SST, and that the time to reach the maximum intensity is shorter (Figs. 2a, b), although the tracks in these experiments are similar (Fig. 1b). Note that there are different ways to measure TC size. In this paper, we use the radius where the azimuthally-averaged 10-m sustained wind exceeds 17 m s^{-1} (R17) to determine TC size. As can be seen in Fig. 2c, the TC size increases with SST. This is consistent with the case-study results of Sun et al. (2017b), which showed that the ACI (the area contained within the outermost enclosed isobaric line at the surface) and A17 (the area under R17) increase with SST.

TC size can be seen from surface wind profile, and is determined by TC intensity (i.e., MWS), TC inner size [i.e., the radius of maximum wind (RMW)], and the outer slope. Figure 3 demonstrates the time-averaged wind profile at 10-m during the TC mature stage, which is defined as the period when the maximum 10-m wind speed is close to its lifetime maximum 10-m wind speed. As SST increases, TC intensity in the sensitivity experiments is greatly enhanced compared to that in CTRL. As expected, the TC outer size, in terms of the radius of gale-force wind (17 m s^{-1}), increases significantly with the increase of SST. As is shown, the wind profile is not particularly smooth in the outer area of TC, because the wind speed in the outer zone is not only related to the MWS, but also affected by the convection in the outer zone; that is, the development of convection in the outer zone will also affect the area covered by the gale-force wind (this area is referred to as A17). In summary, in the wind profile diagram, except for TC intensity, the wind outside the RMW is an important reason for TC size increase with ocean warming. Next, we will study how ocean warming affects TC size via changing outer wind profile.

Emanuel (1986) pointed out that the heat transfer from the ocean to the atmosphere plays an important role in determining TC convection intensity and the extent of its eyewall, which ultimately affects the strength and size of the TC. In our sensitivity runs, the SST is increased uniformly over the whole WNP. The SST increases by 1−4°C, which theoretically allows the atmosphere to obtain more SEF from the ocean, where SEF is the sum of latent heat (LH) and sensible heat (SH) fluxes. We study how the difference in SST will affect TC size when all other conditions are kept the same. Different SSTs could lead to changes not only in temperature difference but also in moisture difference between ocean surface and the air above, which then cause changes to SEF. It is noteworthy that previous studies have mentioned the effects of SST, SEF, and air–sea moisture difference (ASMD) on TC intensity, but seldom paid attention to the effect of ocean warming on TC outer convection and thus outer wind that eventually leads to the increase of TC size. We divide SST into SST in the inner region and

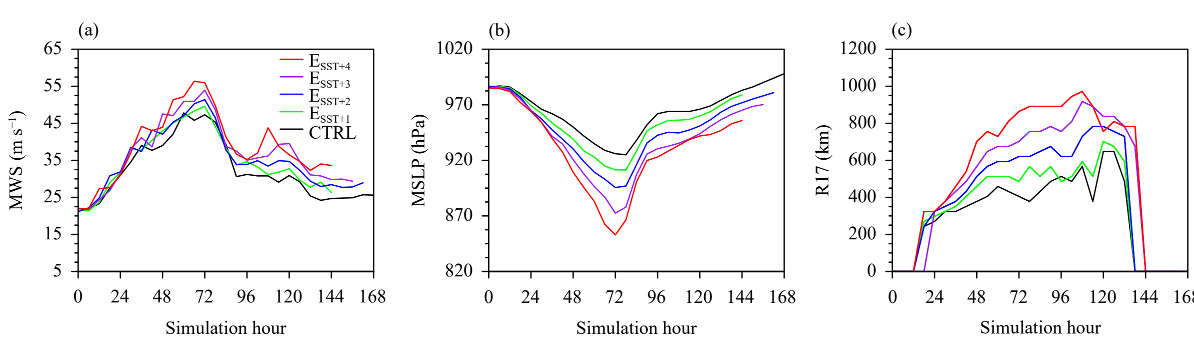

Fig. 2. Temporal evolutions of (a) maximum wind speed (MWS), (b) minimum sea level pressure (MSLP), and (c) radius of > 17 m s^{-1} azimuthal mean 10-m wind speed (R17) in SST sensitivity experiments. Black curve denotes CTRL, while green, blue, purple, and red curves denote E_{SST+1}, E_{SST+2}, E_{SST+3}, and E_{SST+4}, respectively.

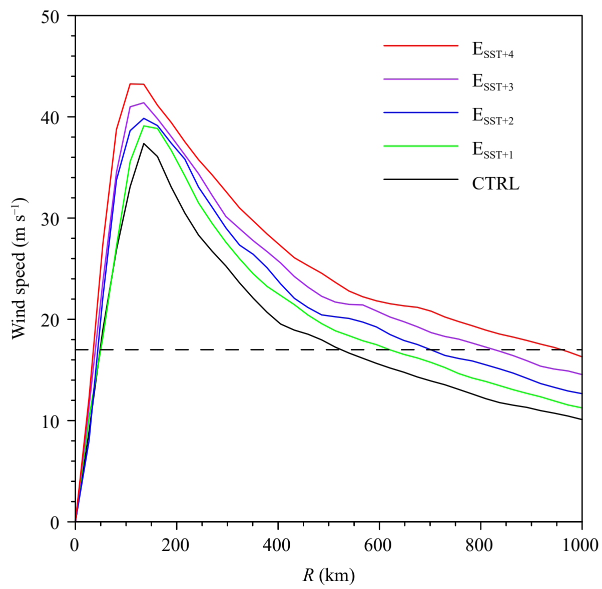

Fig. 3. Radial distributions of 10-m azimuthal mean wind speed during the TC mature stage in sensitivity experiments. The dashed line indicates 17 m s^{-1}. TC mature stage is defined as the period when the maximum 10-m wind speed (V_{max}) is close to its lifetime maximum 10-m wind speed (V_{smax}), i.e., $|V_{max} - V_{smax}| \leqslant 3$ m s^{-1}.

that in the outer region to explain possible mechanism, and emphasize the impact of inner SST on TC intensity and the impact of outer SST on TC size.

Figure 4 shows the temporal evolution of SEF within 0–400 km from the TC center in CTRL and in E$_{SST+1}$, E$_{SST+2}$, E$_{SST+3}$, and E$_{SST+4}$. For the TC in CTRL, the simulated SEF is mainly concentrated in the inner region near the radius of 100–200 km, and increases with time. The increased SEF near the eyewall favors the development of TC during its intensifying period. In the sensitivity experiments of E$_{SST+1}$, E$_{SST+2}$, E$_{SST+3}$, and E$_{SST+4}$, following the increase of SST, the simulated SEF not only becomes larger but also wider, eventually contributing to a stronger TC through inputting more energy into the TC eyewall (inner region) and a larger TC through inputting more energy into the TC outer spiral rainbands (outer region). This can be easily found in Fig. 4f, which shows that warmer experiments with more SEF in the inner and outer regions have a more favorable condition for the development and expansion of TC with respect to CTRL.

Next, we discuss the impact of ocean warming on SEF. The SEF (i.e., the sum of LH and SH fluxes) is controlled by three variables: (1) the temperature difference between surface ocean and the air above, (2) the moisture difference between surface ocean and the air above, and (3) surface wind speed (Malkus and Riehl, 1960).

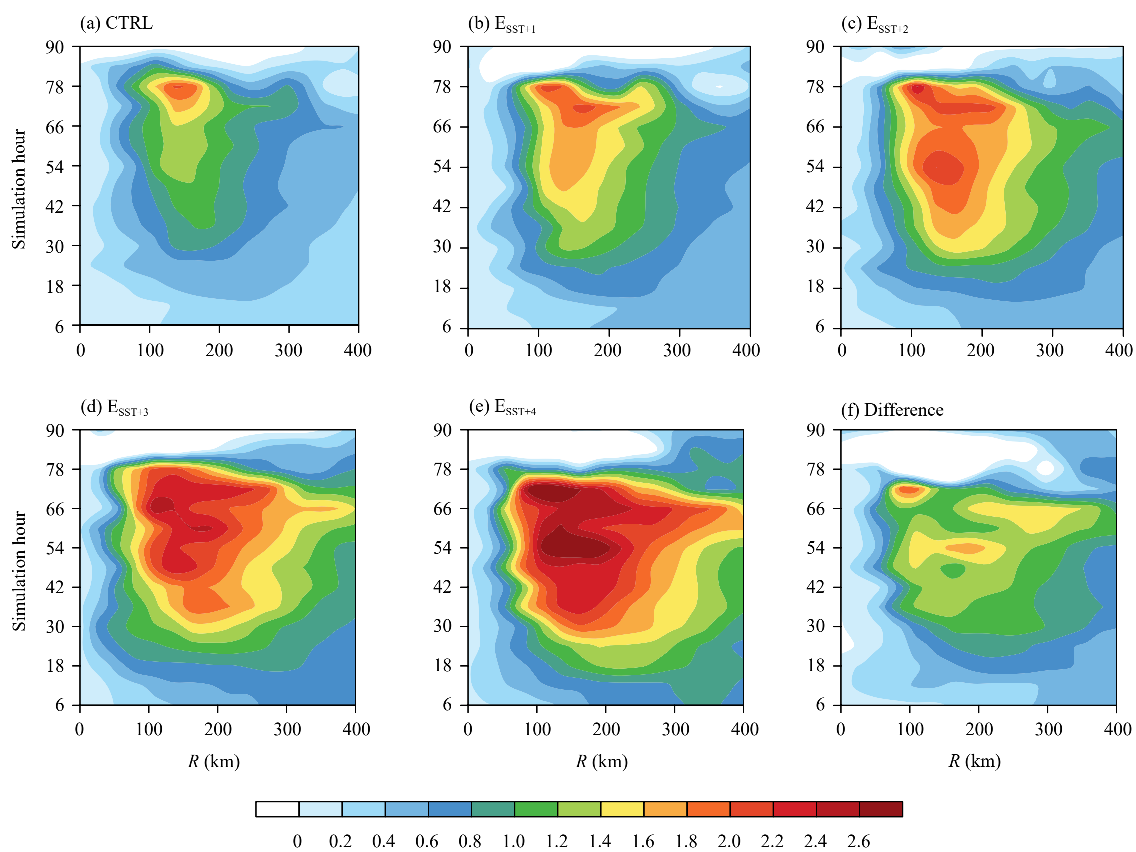

Fig. 4. Temporal–radial distributions of azimuthally-averaged surface entropy flux (SEF; 10^3 W m^{-2}) from (a) CTRL and (b−e) E$_{SST+1}$, E$_{SST+2}$, E$_{SST+3}$, and E$_{SST+4}$, respectively. The panel (f) shows the difference between E$_{SST+4}$ and CTRL (E$_{SST+4}$ minus CTRL).

During the initial period, the differences in wind field among different experiments are small. The difference in LH and SH is mainly due to air–sea moisture difference and air–sea temperature difference (ASTD). With the uniform increase of SST, both ASMD and ASTD increase at the same time in the inner and outer regions of the TC, so the SEF in the inner region and that in the outer region will increase significantly. Since LH is much larger than SH, we focus on the ASMD that affects LH rather than the ASTD that is closely related to SH. For the warmer SST experiment (i.e., E_{SST+4}), the ASMD is larger than that in CTRL at the initial time due to the large increase in SST (see Figs. 5a–e). During the period of TC developing into its maturity (i.e., 30–70 h), the ASMD distributions in the inner and outer regions are changing. The difference map of E_{SST+4} and CTRL (Fig. 5f) shows that the ASMD difference in the outer area is significantly larger than that in the inner area. The reason for the pattern difference of ASMD is that specific humidity at 2 m is larger in the inner zone than in the outer zone because air inflow transports a large amount of water vapor to the inner region (figure omitted). Through the ocean's energy input into the atmosphere (namely, SEF), the convection outside the TC is gradually developed, the local near-surface pressure becomes lower, the local horizontal pressure gradient increases, and thus the horizontal tangential wind in the outer region is enhanced (see Fig. 6), which then feeds back to the SEF for further increase, forming a positive feedback. This makes the convection in the TC outer region develop rapidly, which leads to an increase in TC size. However, the ASMD in the outer area of CTRL is small, which is not enough to excite strong convection in the outer zone; so, there is no positive feedback favorable for increasing TC size. The azimuthally-averaged convective available potential energy (CAPE) in the mature stage is plotted (Fig. 7). CAPE in CTRL and E_{SST+1} shows low energy in both inner and outer regions. While CAPE values in the warmer SST experiments show more convection energy in the inner and outer regions, with CAPE being generally larger than 2400 and 3000 J kg^{-1}, respectively. However, the effects of CAPE in the inner and outer regions are different. CAPE (Fig. 7) in the inner region is an important reason for TC intensity. The detached inner CAPE can be a trigger for deep convection and further promote TC enhancement. Outer spiral

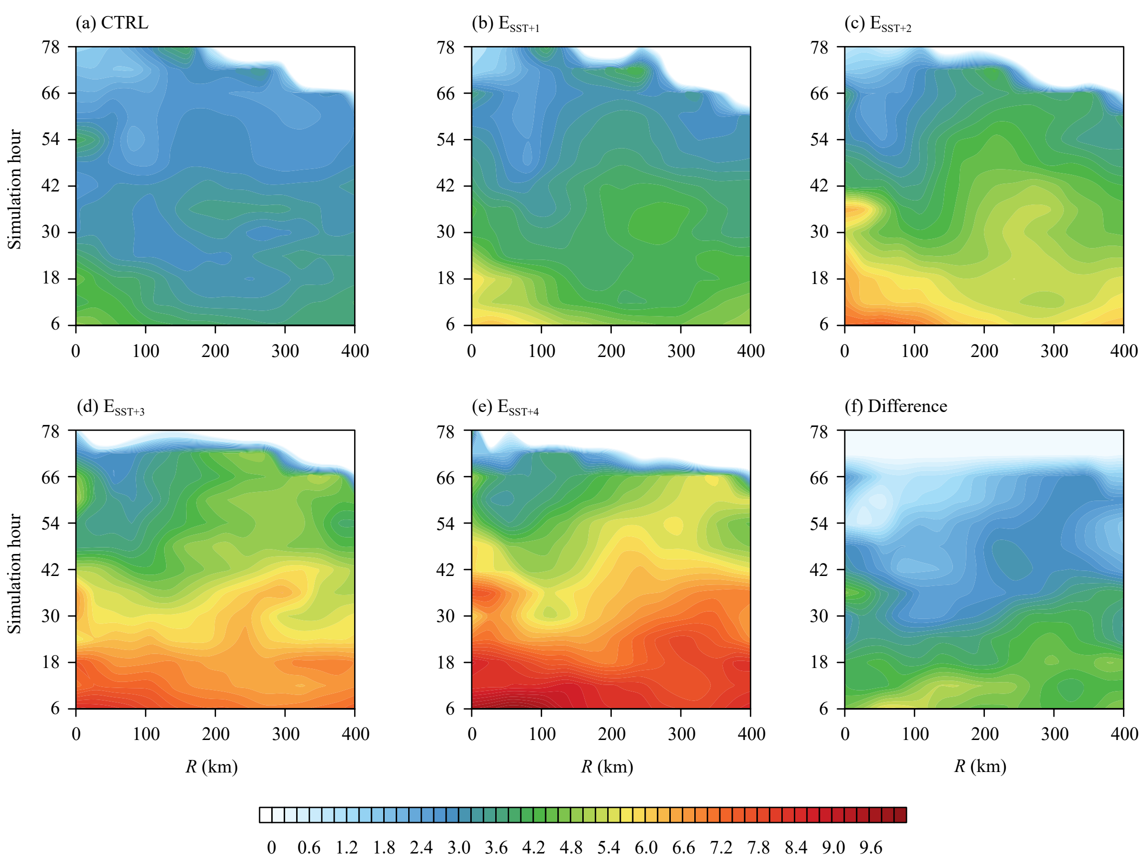

Fig. 5. As in Fig. 4, but for air–sea moisture difference (ASMD; 10^3 W m^{-2}).

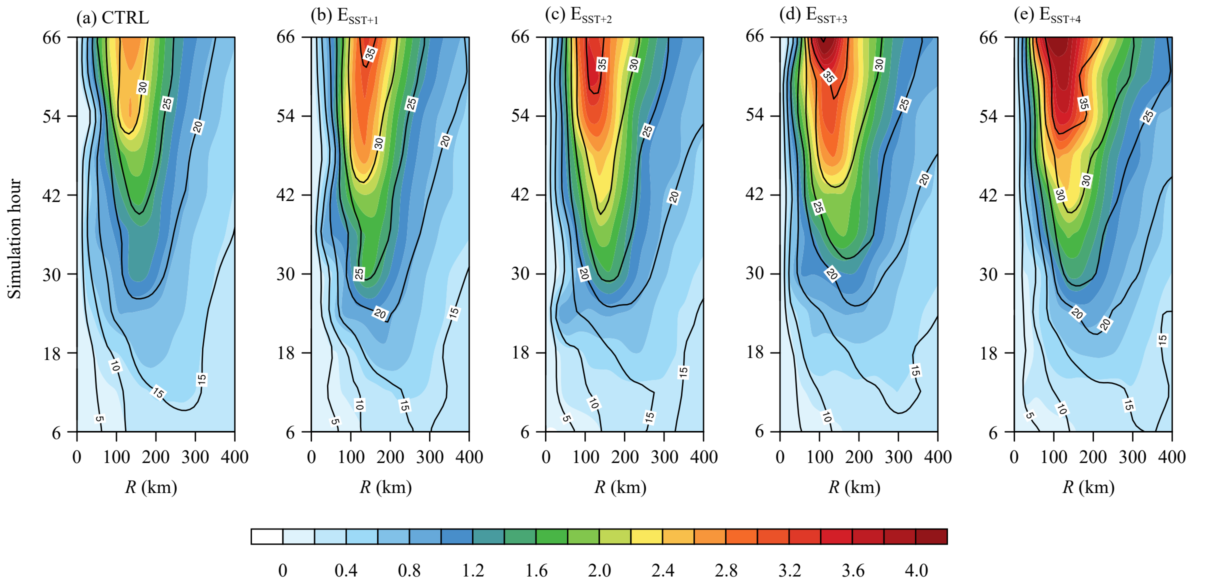

Fig. 6. Temporal–radial distributions of radial sea level pressure gradient (shading; 10^{-2} Pa m^{-1}) and tangential wind at 10 m (contour; m s^{-1}) from (a) CTRL and (b−e) E_{SST+1}, E_{SST+2}, E_{SST+3}, and E_{SST+4}, respectively.

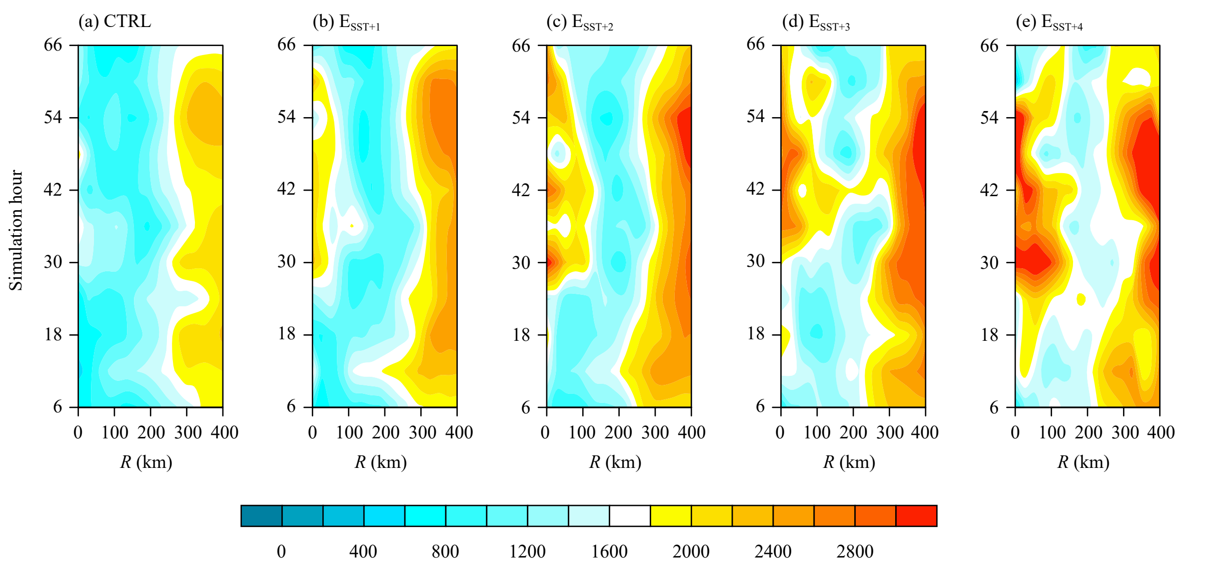

Fig. 7. Temporal–radial distributions of azimuthally-averaged convective available potential energy (CAPE; J kg^{-1}) from (a) CTRL and (b−e) E_{SST+1}, E_{SST+2}, E_{SST+3}, and E_{SST+4}, respectively.

rainbands can be reorganized if the ambient outer CAPE is large, which means that the enhanced CAPE is thermodynamically helpful for maintaining the convection in the outer region.

Although the increase of SST favors both TC intensity and size simultaneously, TC size and TC intensity are quite independent in the inner and outer regions; that is, TC size is only weakly correlated with TC intensity (Liu and Chan, 1999). On the one hand, the increase of SEF will increase TC intensity by enhancing the convection near the inner eyewall. On the other hand, SEF will facilitate the convection development in the outer zone and thus increase TC size. Specifically, the SST increase in the outer zone makes the stratification there unstable, which is conducive to the development of convection. As shown by the temporally averaged vertical velocity (contour) in Fig. 8, in addition to the strong ascending motion in the TC inner region, the sensitivity experiments under warmer SSTs also show ascending motion in the outer region of the TC. In the warmer SST experiments, when the TC develops into its maturity stage, convection occurs in the outer zone. Correspondingly, outer spiral

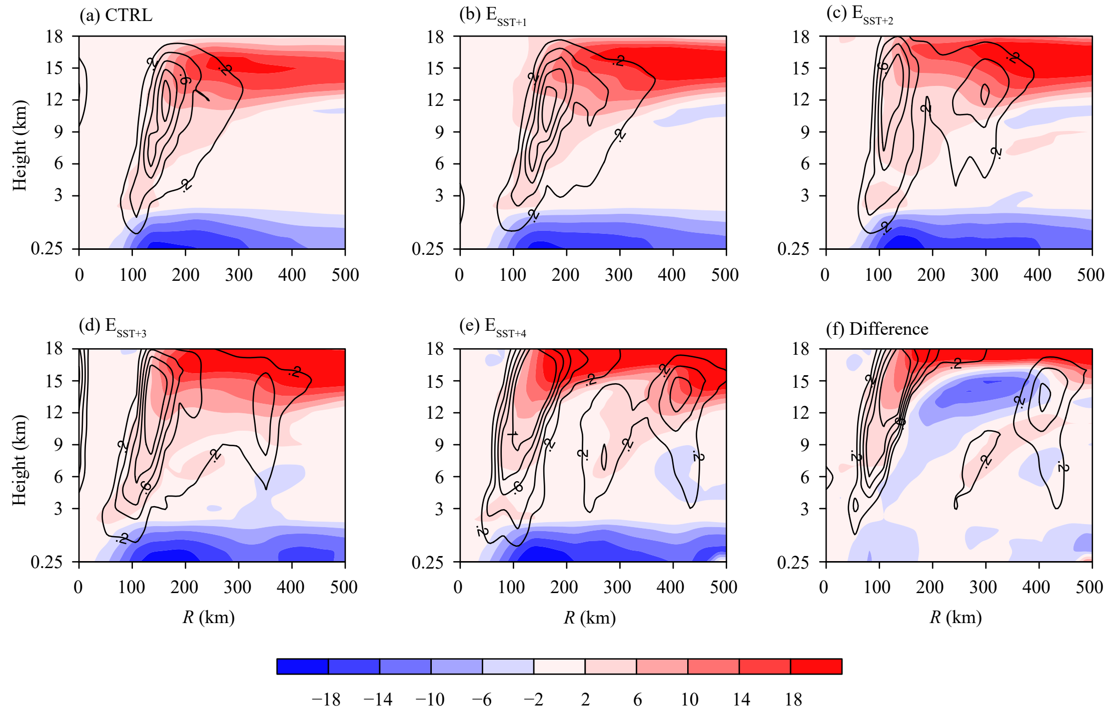

Fig. 8. Height–radiau cross-sections of azimuthally-averaged radial-wind circulation (shading; m s^{-1}) and vertical wind velocity (contour; m s^{-1}) at the mature stage from (a) CTRL and (b–e) E_{SST+1}, E_{SST+2}, E_{SST+3}, and E_{SST+4}, respectively. The panel (f) shows the difference between E_{SST+4} and CTRL (E_{SST+4} minus CTRL).

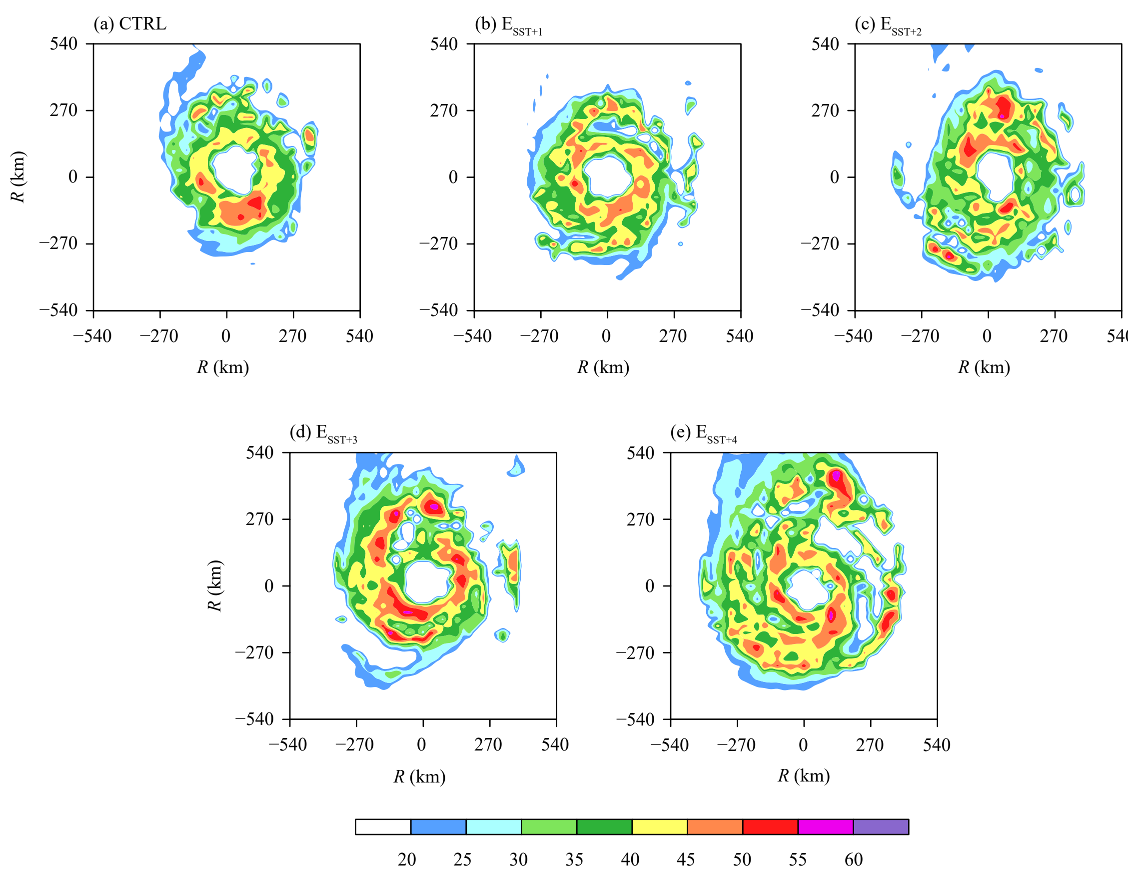

Fig. 9. Distributions of maximum reflectivity (dBZ) at the mature stage: (a) CTRL and (b–e) E_{SST+1}, E_{SST+2}, E_{SST+3}, and E_{SST+4}, respectively.

rainbands (Figs. 9c–e) gradually develop in the warmer experiments. In Fig. 9, TC size can also be seen to increase with the increased SST according to maximum reflectivity. When the SST in the outer region is warmed up and SEF is increased, more water vapor and heat are transported from the ocean into the atmosphere, which makes the outer region more unstable, and there is a convergence in the lower layer, which is beneficial to enhancing the inflow. Xu and Wang (2010a) pointed out that the increase in inflow will increase the tangential wind, which further enhances SEF.

Many studies (e.g., Xu and Wang, 2010b; Stovern and Ritchie, 2016) have shown that the radial distribution of SEF contributes greatly to tangential wind, and that the increase of tangential wind further enhances SEF, which forms a positive feedback. This positive feedback mechanism can be used to explain why TC size increases with ocean warming. As shown in Figs. 4, 8, the SEF in the outer zone is larger in the sensitivity experiments than in CTRL, the radial inflow develops due to the convection in the outer zone, and a high-value area appears in the vicinity of 400–500 km. All these contribute to the expansion of tangential wind (Fig. 6), which is beneficial to the expansion of wind strength-related radius and therefore the increase of TC size.

To further understand the processes associated with TC size change, we conduct azimuthal-mean tangential wind budget following Persing et al. (2002) and Wang et al. (2016). The budget equation can be written as,

$$\frac{\partial \bar{v}}{\partial t} = -\bar{u}\overline{\zeta_{\text{abs}}} - \bar{w}\frac{\partial \bar{v}}{\partial z} - \overline{u'\zeta'_{\text{abs}}} - \overline{w'\frac{\partial v'}{\partial z}} + \bar{F}, \tag{6}$$

where u, v, and w are the radial, tangential, and vertical winds, respectively; ζ_{abs} is absolute vorticity; and F includes friction and vertical mixing. The overbar denotes azimuthal mean, and the prime denotes deviation from the azimuthal mean. The five terms on the right-hand side of Eq. (6) are mean radial advection, mean vertical advection, eddy radial advection, eddy vertical advection, and friction, respectively.

The azimuthal-mean tangential wind budget is computed during the TC size change period from 48 to 54 h (Fig. 10). The left column of Fig. 10 represents the total tangential wind tendency, and the right column represents mean radial advection. Clearly, the tangential wind tendency is mainly contributed by azimuthally mean radial advection, and the other terms have negative contributions or are small in magnitude (not shown). The mean radial advection accelerates the tangential wind in the lower troposphere, but decelerates the tangential wind in the inner region above the inflow. With SST increasing, the mean radial advection in the boundary layer becomes larger. The maximum range is expanded from 100 to 200 km, which is favorable for the increase of tangential wind tendency according to Eq. (6). As a result, the TC size increases.

3.2 *Sensitivity of PDI and PDS to ocean warming*

Here, we focus on the impact of ocean warming on PDI and PDS changes. Figure 11 shows the changes in PDI and PDS as well as the rescaled TC lifetime (*L*), intensity (*I*), and size (*S*) in response to SST increase. With the linear increase of SST, the growth rates of PDI and PDS differ, which is consistent with the results of Sun et al. (2017a). The growth rate of PDS is larger than that of PDI: PDI increases linearly at approximately 0.3×10^{10} $m^3\ s^{-2}$ per 1°C SST increase, while PDS increases exponentially at about 45% per 1°C SST increase. Consistent with Figs. 2, 3, 9, the rescaled TC intensity *I* and size *S* both increase in response to increasing SST, with the change rate of *S* more prominent; while the rescaled TC lifetime *L* maintains or slightly decreases in the sensitivity experiments. Many theoretical and experimental studies have shown that ocean warming will increase TC size (e.g., Sun et al., 2013, 2014, 2017a; Radu et al., 2014; Wang et al., 2015). Thus, the change in TC size should be considered when estimating potential destruction of TC in the context of global warming.

Table 1 lists the relative contributions to PDS by different terms/factors with respect to CTRL. The method of calculating the relative contributions is introduced by Emanuel (2007) and used by Lin et al. (2015) and others. The percentage in the table shows the contribution of an individual factor to the increase of potential destructive power when TC size change is considered. Clearly, the relative contribution by rescaled TC size dominates those by rescaled TC lifetime and intensity. Specifically, when SST increases by 1–4°C, the relative contribution to PDS by rescaled TC lifetime (*L*) is negative, while those by rescaled TC intensity (*I*) and rescaled TC size (*S*) are positive. More importantly, the contribution by rescaled TC size is always greater than 70%.

The increase of term *S* is the main reason for the increase of PDS under warmer SST, while the contribution of terms *L* and *I* to the increase of PDS varies. There are significant changes of different terms/factors between SST increase of 1°C and that of 2°C. When the SST is increased by 1°C, the decrease in term *L* has a greater contribution to the increase in PDS, and the contribution of term *I* reaches about 50%. When the SST is increased by 2°C, the change is more obvious. Term *L* has almost no contribution to the increase of PDS, and the contribu-

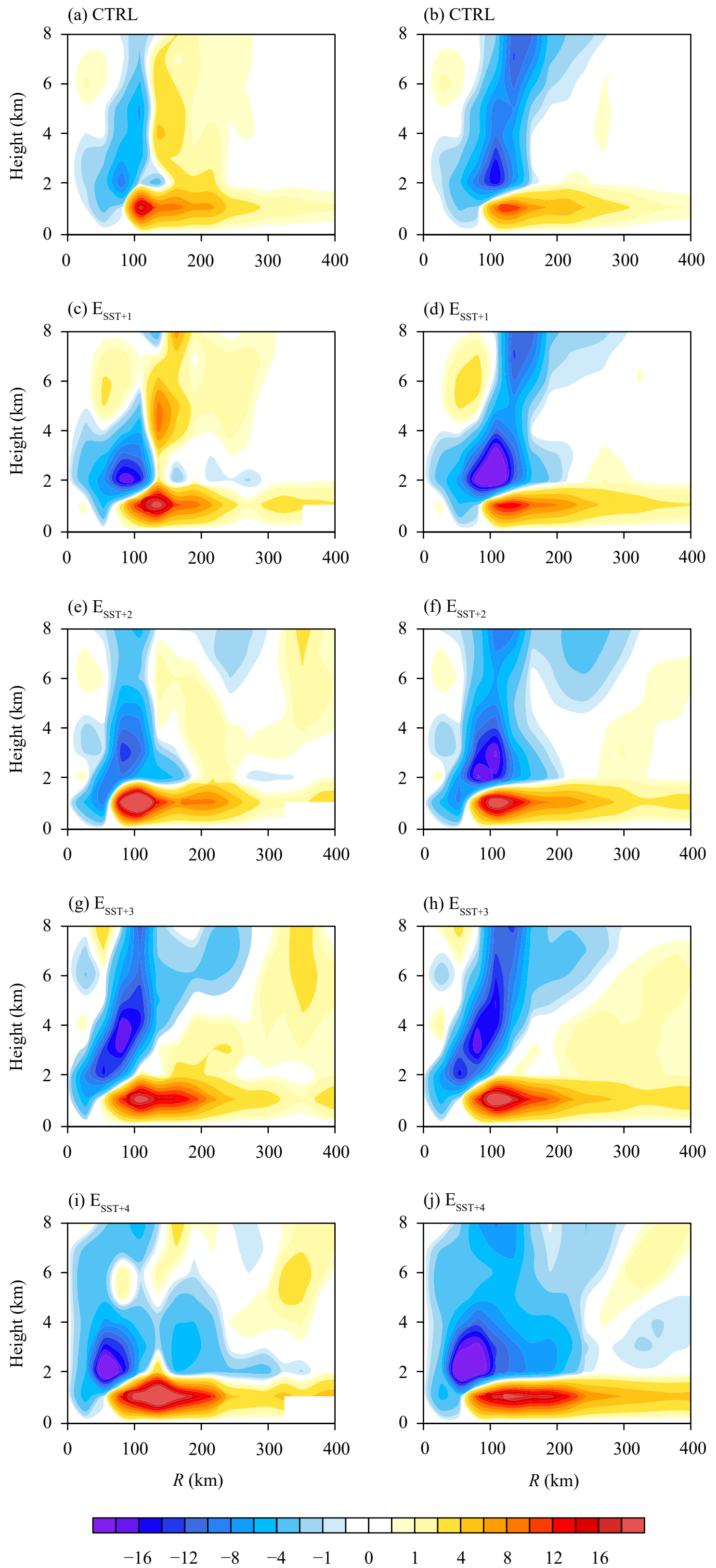

Fig. 10. Height–radius cross-sections of diagnosed tangential wind tendency (sum of the five terms; m s^{-1} h^{-1}) averaged from 48 to 54 h during the TC size change period for CTRL, E_{SST+1}, E_{SST+2}, E_{SST+3}, and E_{SST+4} (left panels). Right panels are the same as the left panels, except for mean radial advection (m s^{-1} h^{-1}).

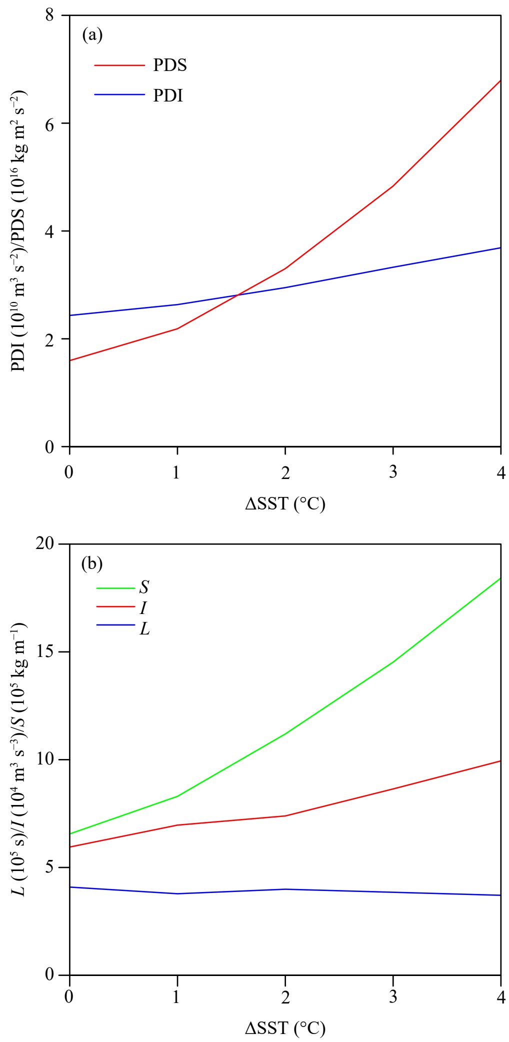

Fig. 11. (a) PDI (blue) and PDS (red) as a function of SST increase (ΔSST). (b) Rescaled TC lifetime (*L*, blue), intensity (*I*, red), and size (*S*, green) as a function of ΔSST.

Table 1. Contributions to PDS change by different terms/factors with respect to CTRL. ΔSST is SST change. Specifically, the relative contribution of term *L*, for example, is computed as $[\ln(L_E) - \ln(L_C)]$ / $[\ln(PDS_E) - \ln(PDS_C)]$, in which subscripts $_E$ and $_C$ denote sensitivity and control experiment, respectively

Exp.	ΔSST (°C)	Contribution (%) to PDS change		
		Term *L*	Term *I*	Term *S*
E_{SST+1}	1	–24.9	50.1	74.8
E_{SST+2}	2	–3.4	29.8	73.5
E_{SST+3}	3	–5.5	33.7	71.8
E_{SST+4}	4	–6.7	35.4	71.3

tion by term *I* is reduced by about 20%. After every 1°C increase in SST for SST increase range of 3–4°C, the contributions of terms *L* and *S* are almost unchanged. In summary, TC size plays a major role in the increase of PDS, while the contributions of TC lifetime and intensity are small.

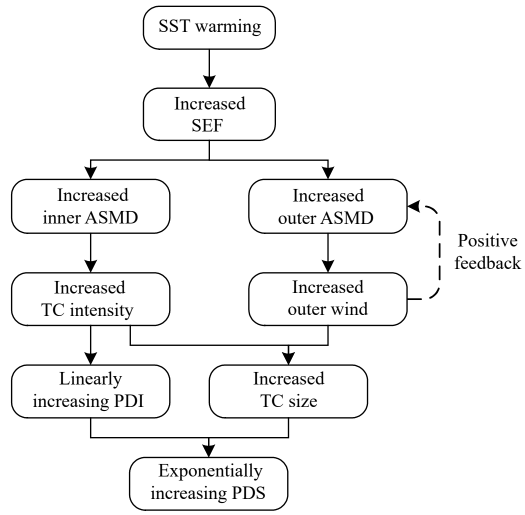

Fig. 12. Schematic diagram on possible mechanisms responsible for the increase of TC destructive potential (PDI and PDS) under ocean warming.

A schematic diagram (Fig. 12) is drawn to illustrate possible mechanisms for the increase of TC destructive potential (i.e., PDI and PDS) under ocean warming. Increasing SST uniformly by 1–4°C in the entire WNP will increase inner and outer ASMD and thus SEF, especially those in the outer region. The increase of SEF in the inner region will increase TC intensity by enhancing the convection near the eyewall, while the increase of SEF in the outer region will cause the development of outer convection. Through the positive feedback of outer SEF and wind speed, TC size increases, which causes TC destructive potential to grow exponentially. Further, TC size change affects TC destructive potential change. It is worth noting that the idealized experiments based on the present-day climatology can more reasonably and universally explain the mechanism of TC size change under ocean warming compared with the experiments using real TC cases.

4. Summary and discussion

We design CTRL and four sensitivity experiments to investigate TC response to SST increase under the present-day climate condition, with a focus on TC potential destructiveness. The goal of this study is to shed light on possible effects of ocean warming and thus global warming on TC activity and destructiveness. According to the calculation of PDS, the increase in TC size in response to SST increase is the main factor causing an exponential increase in TC potential destructiveness. The mechanism behind the increase in TC size due to SST increase is critical to our understanding of the impact of ocean warming on TC potential destructiveness. Ocean warming will increase ASMD during the initial development stage of TC, especially for ASMD in the outer region. When the TC develops, ASMD between CTRL and E_{SST+4} (E_{SST+4} minus CTRL) shows that after 30 h of integration, ASMD in the periphery of the TC is larger than that in the interior, which expands the TC convective zone outward. For the simulations with larger SST increase, ASMD in the outer zone increases the SEF of the TC by transferring energy upwards. The radial distribution of SEF will make the tangential wind stronger via diabatic heating, thus facilitating the expansion of gale-force wind radius; eventually, the TC size increases. Simultaneously, the increase of SEF will increase TC intensity by enhancing the convection near the eyewall, which makes a linear increase in TC potential destructiveness. Previous studies indicated that TC intensity, and thus its size, is sensitive to increased SST due to increased SEF and thus stronger latent energy transfer inputting into the TC inner region (e.g., TC eyewall), but they ignored the weak statistical relationship between TC intensity and TC size and did not realize the importance of SEF spatial distribution on TC size. In this study, we mainly focus on ASMD in the outer region and thus the increased outer tangential wind. We emphasize the effect of ocean warming on the radial distribution of ASMD, TC outer convection, outer tangential wind, and thus the increase of TC size.

When considering the impact of global warming on TC activity, the change of TC size is important, as demonstrated here once again. In recent years, thanks to the improvement of observational methods, some meteorological agencies have begun to include TC size data to their observation data collection, which will greatly help estimate TC destructive potential more accurately. Global warming is more than just ocean warming; it changes large-scale circulation fields as well. Possibly, the change of TC destructive potential will be a little different under global warming when using CMIP5 model outputs as initialization conditions, which is not considered in this study and will be investigated in future.

REFERENCES

Bacmeister, J. T., K. A. Reed, C. Hannay, et al., 2018: Projected changes in tropical cyclone activity under future warming scenarios using a high-resolution climate model. *Climatic Change*, **146**, 547–560, doi: 10.1007/s10584-016-1750-x.

Chan, J. C. L., and K. S. Liu, 2004: Global warming and western North Pacific typhoon activity from an observational perspective. *J. Climate*, **17**, 4590–4602, doi: 10.1175/3240.1.

Chan, K. T. F., and J. C. L. Chan, 2015: Impacts of vortex intensity and outer winds on tropical cyclone size. *Quart. J. Roy. Meteor. Soc.*, **141**, 525–537, doi: 10.1002/qj.2374.

Chavas, D. R., N. Lin, W. H. Dong, et al., 2016: Observed tropical cyclone size revisited. *J. Climate*, **29**, 2923–2939, doi: 10.1175/JCLI-D-15-0731.1.

Chou, M.-D., and M. J. Suarez, 1994: An Efficient Thermal Infrared Radiation Parameterization for Use in General Circulation Models. NASA Technical Memorandum No. 104606, NASA, Washington, 85 pp.

Deo, A. A., D. W. Ganer, and G. Nair, 2011: Tropical cyclone activity in global warming scenario. *Nat. Hazards*, **59**, 771–786, doi: 10.1007/s11069-011-9794-8.

Emanuel, K. A., 1986: An air-sea interaction theory for tropical cyclones. Part I: Steady-state maintenance. *J. Atmos. Sci.*, **43**, 585–605, doi: 10.1175/1520-0469(1986)043<0585:AASITF>2.0.CO;2.

Emanuel, K., 2005: Increasing destructiveness of tropical cyclones over the past 30 years. *Nature*, **436**, 686–688, doi: 10.1038/nature03906.

Emanuel, K., 2007: Environmental factors affecting tropical cyclone power dissipation. *J. Climate*, **20**, 5497–5509, doi: 10.1175/2007JCLI1571.1.

Hill, K. A., and G. M. Lackmann, 2009: Influence of environmental humidity on tropical cyclone size. *Mon. Wea. Rev.*, **137**, 3294–3315, doi: 10.1175/2009MWR2679.1.

Hong, S.-Y., J. Dudhia, and S.-H. Chen, 2004: A revised approach to ice microphysical processes for the bulk parameterization of clouds and precipitation. *Mon. Wea. Rev.*, **132**, 103–120, doi:10.1175/1520-0493(2004)132<0103:ARATIM>2.0.CO;2.

Kain, J. S., 2004: The Kain–Fritsch convective parameterization: An update. *J. Appl. Meteor.*, **43**, 170–181, doi: 10.1175/1520-0450(2004)043<0170:TKCPAU>2.0.CO;2.

Klotzbach, P. J., 2006: Trends in global tropical cyclone activity over the past twenty years (1986–2005). *Geophys. Res. Lett.*, **33**, L10805, doi: 10.1029/2006GL025881.

Knutson, T. R., J. L. McBride, J. Chan, et al., 2010: Tropical cyclones and climate change. *Nat. Geosci.*, **3**, 157–163, doi: 10.1038/ngeo779.

Li, H., and R. L. Sriver, 2018: Impact of tropical cyclones on the global ocean: Results from multidecadal global ocean simulations isolating tropical cyclone forcing. *J. Climate*, **31**, 8761–8784, doi: 10.1175/JCLI-D-18-0221.1.

Li, T., M. H. Kwon, M. Zhao, et al., 2010: Global warming shifts Pacific tropical cyclone location. *Geophys. Res. Lett.*, **37**, L21804, doi: 10.1029/2010gl045124.

Lighthill, J., G. Holland, W. Gray, et al., 1994: Global climate change and tropical cyclones. *Bull. Amer. Meteor. Soc.*, **75**, 2147–2157, doi: 10.1175/1520-0477-75.11.2147.

Lin, I.-I., G. J. Goni, J. A. Knaff, et al., 2013: Ocean heat content for tropical cyclone intensity forecasting and its impact on storm surge. *Nat. Hazards*, **66**, 1481–1500, doi: 10.1007/s11069-012-0214-5.

Lin, I.-I., and J. C. L. Chan, 2015: Recent decrease in typhoon destructive potential and global warming implications. *Nat. Commun.*, **6**, 7182, doi: 10.1038/ncomms8182.

Liu, K. S., and J. C. L. Chan, 1999: Size of tropical cyclones as inferred from *ERS-1* and *ERS-2* data. *Mon. Wea. Rev.*, **127**, 2992–3001, doi: 10.1175/1520-0493(1999)127<2992:SOTCAI>2.0.CO;2.

Malkus, J. S., and H. Riehl, 1960: On the dynamics and energy transformations in steady-state hurricanes. *Tellus*, **12**, 1–20, doi: 10.3402/tellusa.v12i1.9351.

Mlawer, E. J., S. J. Taubman, P. D. Brown, et al., 1997: Radiative transfer for inhomogeneous atmospheres: RRTM, a validated correlated-k model for the longwave. *J. Geophys. Res. Atmos.*, **102**, 16,663–16,682, doi: 10.1029/97JD00237.

Persing, J., M. T. Montgomery, and R. E. Tuleya, 2002: Environmental interactions in the GFDL hurricane model for Hurricane Opal. *Mon. Wea. Rev.*, **130**, 298–317, doi: 10.1175/1520-0493(2002)130<0298:EIITGH>2.0.CO;2.

Radu, R., R. Toumi, and J. Phau, 2014: Influence of atmospheric and sea surface temperature on the size of Hurricane Catarina. *Quart. J. Roy. Meteor. Soc.*, **140**, 1778–1784, doi: 10.1002/qj.2232.

Stovern, D. R., and E. A. Ritchie, 2016: Simulated sensitivity of tropical cyclone size and structure to the atmospheric temperature profile. *J. Atmos. Sci.*, **71**, 4553–4571, doi: 10.1175/JAS-D-15-0186.1.

Sun, Y., Z. Zhong, Y. Ha, et al., 2013: The dynamic and thermodynamic effects of relative and absolute sea surface temperature on tropical cyclone intensity. *Acta Meteor. Sinica*, **27**, 40–49, doi: 10.1007/s13351-013-0105-z.

Sun, Y., Z. Zhong, L. Yi, et al., 2014: The opposite effects of inner and outer sea surface temperature on tropical cyclone intensity. *J. Geophys. Res. Atmos.*, **119**, 2193–2208, doi: 10.1002/2013jd021354.

Sun, Y., Z. Zhong, T. Li, et al., 2017a: Impact of ocean warming on tropical cyclone size and its destructiveness. *Sci. Rep.*, **7**, 8154, doi: 10.1038/s41598-017-08533-6.

Sun, Y., Z. Zhong, T. Li, et al., 2017b: Impact of ocean warming on tropical cyclone track over the western North Pacific: A numerical investigation based on two case studies. *J. Geophys. Res. Atmos.*, **122**, 8617–8630, doi: 10.1002/2017jd026959.

Taylor, K. E., R. J. Stouffer, and G. A. Meehl, 2012: An overview of CMIP5 and the experiment design. *Bull. Amer. Meteor. Soc.*, **93**, 485–498, doi: 10.1175/BAMS-D-11-00094.1.

Trenberth, K. E., L. J. Cheng, P. Jacobs, et al., 2018: Hurricane Harvey links to ocean heat content and climate change adaptation. *Earth's Future*, **6**, 730–744, doi: 10.1029/2018ef000825.

Walsh, K. J. E., J. L. McBride, P. J. Klotzbach, et al., 2015: Tropical cyclones and climate change. *Wiley Interdiscip. Rev.: Climate Change*, **7**, 65–89, doi: 10.1002/wcc.371.

Wang, H., C.-C. Wu, and Y. Q. Wang, 2016: Secondary eyewall formation in an idealized tropical cyclone simulation: Balanced and unbalanced dynamics. *J. Atmos. Sci.*, **73**, 3911–3930, doi: 10.1175/JAS-D-15-0146.1.

Wang, S., R. Toumi, A. Czaja, et al., 2015: An analytic model of tropical cyclone wind profiles. *Quart. J. Roy. Meteor. Soc.*, **141**, 3018–3029, doi: 10.1002/qj.2586.

Webster, P. J., G. J. Holland, J. A. Curry, et al., 2005: Changes in tropical cyclone number, duration, and intensity in a warming environment. *Science*, **309**, 1844–1846, doi: 10.1126/science.1116448.

Xu, J., and Y. Q. Wang, 2010a: Sensitivity of tropical cyclone inner-core size and intensity to the radial distribution of surface entropy flux. *J. Atmos. Sci.*, **67**, 1831–1852, doi: 10.1175/2010JAS3387.1.

Xu, J., and Y. Q. Wang, 2010b: Sensitivity of the simulated tropical cyclone inner-core size to the initial vortex size. *Mon. Wea. Rev.*, **138**, 4135–4157, doi: 10.1175/2010MWR3335.1.

Zhang, C. X., and Y. Q. Wang, 2017: Projected future changes of tropical cyclone activity over the western North and South Pacific in a 20-km-mesh regional climate model. *J. Climate*, **30**, 5923–5941, doi: 10.1175/JCLI-D-16-0597.1.

Tech & Copy Editor: Qi WANG and Lan YI